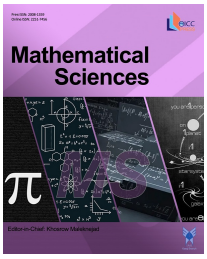

Math. Sci. 2026; 20(3): 281-292

Mathematical Sciences (MS)

https://doi.org/10.57647/mathsci.2026.2003.18

Research Article

Heat Transfer Investigation of Dissipative Couple Stress Rotating Fluid: Numerical and Theoretical Treatments

Mohamed M. Khader[1], Mohamed Adel[2,*], Amel A. Alaidrous[3]

[1]*Department of Mathematics and Statistics, College of Science, Imam Mohammad Ibn Saud Islamic University (IMSIU), Riyadh, Saudi Arabia*

[2]*Department of Mathematics, Faculty of Science, Islamic University of Madinah, Medina, Saudi Arabia*
[3]*Department of Mathematics, Faculty of Sciences, Umm Al-Qura University, Makkah, Saudi Arabia*

[*]**Corresponding author:** adel@sci.cu.edu.eg

Article History

Received:
25 December 2025
Revised:
27 March 2026
Accepted:
24 April 2026
Published in Issue:
30 September 2026

Abstract:

A comprehensive numerical study is presented to investigate heat transfer in the boundary layer flow of an incompressible fluid with a couple stress resulting from a permeable plate and linear extension. The model accounts for the combined influence of a transverse magnetic field and system rotation, where the inclusion of the Coriolis force introduces an additional rotational resistance that alters the flow structure. Fluid properties and wall permeability are systematically examined to assess their roles in shaping the thermal behavior. The thermal analysis is performed under a prescribed surface temperature condition, allowing for a clear evaluation of heat transport mechanisms. Moreover, the formulation incorporates both viscous dissipation and energy due to couple stresses, which are essential in accurately capturing the physics of such fluids. These considerations are particularly relevant in processes associated with the manufacturing and handling of magnetic materials, where rotational and electromagnetic effects coexist and significantly impact heat transfer characteristics. Similarity transformations create a nonlinear set of coupled ODEs with boundary conditions from the governing equations. The merged Fibonacci-Lucas polynomials (MFLPs) are used as part of the problem-solving strategy, along with the least-squares approximation technique, to simplify the equations that define the mathematical model into a nonlinear system of algebraic equations, then solved by Newton iteration approach. The research also includes examining the convergence and estimating the error of the proposed scheme. The results reveal that increasing the couple stress factor can slightly enhance skin friction (3.5%) but significantly reduces heat transfer (26.7%), while increasing the magnetic field parameter markedly decreases both skin friction (50.4%) and heat transfer (23.9%). The discussion revolves around how relevant parameters affect the fluid's temperature and velocity profiles. The technique's effectiveness is shown through a table comparison, indicating good alignment with existing data and highlighting its accuracy.

Keywords: Coriolis force; MHD; Couple stress fluid; Viscous dissipation; Merged Fibonacci-Lucas polynomials

Cite this article: Khader M.M., Adel M., Alaidrous A. Heat Transfer Investigation of Dissipative Couple Stress Rotating Fluid: Numerical and Theoretical Treatments Math. Sci 2026; *20*(3): 281-292 https://doi.org/10.57647/mathsci.2026.2003.18

Nomenclature

x, y	Cartesian coordinates (m)
K	Rotation factor
b	Positive constant $(\frac{1}{s})$
k	Dimensionless temperature index factor
B_0	Magnetic field strength (T)
Pr	Prandtl number
f	Dimensionless stream function

Nomenclature

Cf_x	Dimensionless skin-friction coefficient
Nu_x	Dimensionless Nusselt number
M	Magnetic field parameter
c_p	Specific heat at constant pressure $(J\,kg^{-1}\,K^{-1})$
v_w	Suction velocity $(s^{-1}\,m)$
Ec	Eckert number
T_∞	Ambient temperature (K)

Nomenclature

T_w Temperature of the fluid along the sheet (K)
u, v $x-$ and $y-$velocity components, respectively (ms^{-1})

Greek symbols

κ Thermal conductivity ($m^{-1}\,W\,K^{-1}$)
η Similarity variable
σ Electrical conductivity ($\frac{S}{m}$)
ν Kinematic viscosity ($\frac{m^2}{s}$)
θ Dimensionless temperature
β Couple stress parameter
Γ Suction parameter
μ Coefficient of viscosity ($s^{-1}\,m^{-1}\,kg$)
ξ Material couple stress variable ($\frac{N}{m}$)
λ The energy couple stress parameter
ρ Density of nanofluid ($m^{-3}\,kg$).

1. Introduction

Non-Newtonian fluids encompass a wide range of models that capture complex rheological behaviors such as elasticity, shear-dependent viscosity, and microstructural effects, which have attracted significant attention in industrial and manufacturing fields because their diverse applications in polymer processing, biomedical systems, and advanced thermal technologies, thereby driving continuous research and innovation. In this context, Nazar et al. [1] investigated a micropolar fluid model, emphasizing the role of the micro-rotation phenomenon in the stagnation point flow problem past a stretching wall. Ali et al. [2] focused on a Jeffrey fluid model, analyzing hydromagnetic flow and heat transfer (HT) mechanism past an oscillatory stretching sheet. Olkha and Dadheech [3] considered two distinct non-Newtonian fluids under radiative MHD slip flow, highlighting entropy generation aspects. Nabwey et al. [4] discussed a Carreau nanofluid model, incorporating bioconvection and chemical reaction impacts in a magnetized environment. Khader et al. [5] studied a general non-Newtonian nanofluid model, addressing heat generation properties past a nonlinear stretching sheet. More recent contributions by Bilal et al. [6] explored an investigation in a fourth-grade hybrid nanofluid model with gyrotactic microorganisms, while [7] analyzed a non-Newtonian hybrid nanofluid with chemical reactions over a Riga plate. Additionally, [8] investigated a Prandtl-Eyring fluid model with entropy optimization using artificial intelligence techniques, the research in [9] addressed an unsteady micropolar nanofluid model with experimental validation, and [10] examined a tangent hyperbolic nanofluid model with homogeneous and heterogeneous reactions properties. All these studies demonstrate the diversity of non-Newtonian fluid models and their growing relevance in advanced transport phenomena.

The couple stress fluid model is an important class of non-Newtonian models that account for the influence of microstructural impacts through the fluid, particularly the presence of particle interactions and size-dependent behaviors. Unlike classical viscous models, it incorporates the impact of couple stresses, which arise due to the rotational motion of fluid particles and the associated internal moments. This makes the model especially suitable for describing flows involving lubricants, polymeric suspensions, and biological fluids, where microscale interactions cannot be neglected. The foundation of this model was first established by Stokes [11] in 1984, providing a theoretical framework to better capture the behavior of complex fluids with internal rotational resistance. Therefore, subsequent studies have expanded the applicability of this model across various physical scenarios. Naduvinamani et al. [12] examined the impact of surface roughness on squeeze film characteristics within anisotropic porous sheets, highlighting the role of microstructural effects in lubrication systems. Makinde and Eegunjobi [13] investigated MHD couple stress nanofluid flow in a permeable channel, taking into account the entropy generation and nonlinear thermal radiation. Farooq et al. [14] conducted a comparative discussion of the generalized Couette flow model using advanced analytical techniques, demonstrating the effectiveness of different solution approaches. All these contributions underline the versatility and continued relevance of the couple stress model in modern fluid dynamics research.

The Coriolis force is no mere theoretical abstraction; it is a real physical player in fluid model systems, whether we are talking about massive atmospheric currents or rotating engineering components. When you shift your perspective to a rotating frame, this apparent force kicks in, bending the paths of moving fluid particles and reshaping how momentum is distributed through the flow. In nature, it is the hidden hand behind trade winds, cyclones, and ocean currents. In engineering, it shows up everywhere from turbomachinery and rotating disks to the precise workings of Coriolis mass flow meters used in industrial settings. Ignoring it means missing a key piece of the physics, which is why a growing body of research has focused on understanding its impact, not just for the sake of academic curiosity, but because getting the flow right in rotating systems really matters for reliable design. The early research of Koriko et al. [15] revealed that this Coriolis force does more than tweak fluid-flow past curved surfaces, but it fundamentally restructures velocity distributions and flow patterns. The wide range of applications and the multidisciplinary nature of this type of fluid have strongly motivated extensive applied research in recent years ([16]-[17]).

Numerous studies have looked at the standard Fibonacci and Lucas polynomials and their generalization due to their significance. Theoretical conclusions on the SFLPs have been formulated. The scholars in [18] have delineated conclusions on the SFLPs and their relationships with other polynomials, particularly orthogonal polynomials. The investigations extend beyond SFLPs, with numerous scholars keen on introducing and examining various modified and generalized SFLPs sequences. Abd-Elhameed et al. [19] have

streamlined specific radicals by applying two generic kinds of SFLPs. Diverse sequences of the FLPs, together with their generalizations, have been utilized in multiple research projects to address various types of ODEs [20]. Haq and Ali [21] have formulated a numerical solution for a two-dimensional model.

The primary objective of the current study is to investigate a robust numerical framework for solving the nonlinear system governing the proposed model, with particular emphasis on the newly incorporated Coriolis force as a key novel contribution. The analysis systematically examines the combined effects of viscous dissipation and energy-related stresses to provide a deeper understanding of their influence on the flow and transport behavior. Notably, a clear gap exists in the literature regarding the simultaneous treatment of these mechanisms within this configuration, and to the best of the authors knowledge, such an integrated analysis has not been previously reported. This study is expected to provide significant insights into the effect of Coriolis force on fluid flow and heat transfer, highlighting its potential applications in engineering systems such as rotating machinery, geophysical flows, and industrial processes, thereby underlining the practical importance and relevance of the present work.

2. Mathematical formulation

This work investigates the laminar flow properties of a non-Newtonian coupled stress fluid across a stretching sheet, with particular emphasis on the impact of the Coriolis force, which arises from system rotation. This rotational effect is incorporated to capture its significant role in altering the flow structure and transport characteristics. In addition to the Coriolis contribution, the model accounts for energy-related stresses, viscous dissipation, and a spatially varying surface temperature. The stretching sheet is assumed to move with a linear velocity $u = bx$ along the plane $y = 0$, generating a continuously developing boundary layer. Furthermore, the wall temperature is prescribed as $T_w = T_\infty + Ax^k$, where A governs the rate of thermal variation along the sheet (Figure 1). Through this formulation, the study seeks to clarify the interplay between rotational effects and thermophysical mechanisms in shaping the overall fluid behavior. To actively regulate the flow behavior, an external magnetic field with a magnitude of B_0 is supplied to the stretching sheet. The external magnetic field (MF) is analyzed under the hypothesis of a low magnetic Reynolds number, allowing for the disregard of the induced magnetic field due to its minimal impact relative to the applied MF. Its influence is captured in the boundary layer equations, which take the following form ([22], [23]):

$$\frac{\partial u}{\partial x} + \frac{\partial v}{\partial y} = 0, \tag{1}$$

$$\frac{\sigma B_0^2}{\rho}u + \frac{\xi}{\rho}\frac{\partial^4 u}{\partial y^4} + \frac{\partial u}{\partial y}v + \frac{\partial u}{\partial x}u - 2\,\Omega\, u = \nu\frac{\partial^2 u}{\partial y^2}, \tag{2}$$

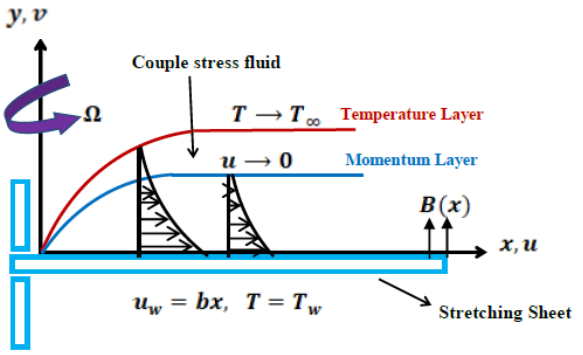

Figure 1. The physical setup of the couple stress model

$$\frac{\partial T}{\partial y}v + \frac{\partial T}{\partial x}u = \frac{\kappa}{\rho c_p}\frac{\partial^2 T}{\partial y^2} + \frac{\nu}{c_p}\left(\frac{\partial u}{\partial y}\right)\left[\left(\frac{\partial u}{\partial y}\right) - \frac{\xi}{\mu\rho}\left(\frac{\partial^3 u}{\partial y^3}\right)\right] + \frac{\xi}{c_p}\left(\frac{\partial^2 u}{\partial y^2}\right)^2. \tag{3}$$

Here, we must mention that the inclusion of the energy due to couple stresses in the energy equation is physically justified as it accounts for the internal rotational interactions within non-Newtonian fluids, such as polymeric and complex fluids, where microstructural effects significantly influence energy transport. Moreover, the viscous dissipation term is incorporated in the same equation due to its important role in high-speed and highly viscous flows, where mechanical energy is converted into thermal energy, thereby affecting the temperature distribution. Therefore, the present configuration is relevant to practical applications, including polymer processing, coating flows, and rotating industrial systems under magnetic environments. A useful simplification arises when the material couple stress variable is set to zero ($\xi = 0$), which effectively reduces the non-Newtonian dipolar fluid to a Newtonian one. In this limit, the influence of coupled stresses vanishes, and the fluid behaves like a standard Newtonian fluid. It is also worth noting the key transport properties: κ denotes the thermal conductivity, and σ the electrical conductivity. To accurately characterize the flow, the following boundary conditions (B.Cs) must be obtained [22]:

$$T = T_w = T_\infty + Ax^k, \quad u = u_w = bx, \quad v = -v_w, \quad \frac{\partial^2 u}{\partial y^2} = 0, \quad at \quad y = 0, \tag{4}$$

$$u \to 0, \quad T \to T_\infty, \quad \frac{\partial u}{\partial y} \to 0, \quad at \quad y \to \infty. \tag{5}$$

The parameter v_w represents the suction velocity and controls the rate at which fluid is either drawn toward or far from the stretching sheet. This, in turn, affects the BL thickness and the overall flow characteristics.

2.1 The dimensionless form of the model

We simplify things by using similarity transformations. This cuts down the number of variables we have to juggle, turning the original PDEs into a set of ODEs that

10.57647/mathsci.2026.2003.18

are dimensionless and much easier to handle. The transformations go like this [24]:

$$\eta = \left(\frac{b\rho}{\mu}\right)^{\frac{1}{2}} y, \qquad u = bx f'(\eta), \tag{6}$$
$$\theta = \frac{T - T_\infty}{T_w - T_\infty}, \qquad v = -\left(\frac{b\mu}{\rho}\right)^{\frac{1}{2}} f(\eta).$$

The governing ODEs, together with their corresponding B.Cs, are presented below, following directly from the similarity transformations (6) discussed earlier. These relations form the backbone of the analysis, as they emerge naturally from the applied transformations.

$$f'(f' - K + M) = f''' - \beta f^{(5)} + f f'', \tag{7}$$

$$PrEcf''\left(\beta f^{(4)} - f''\right) = \theta'' + Pr\left[f\theta' - kf'\theta\right] + Ec\lambda\left(f'''\right)^2, \tag{8}$$

$$f(\eta) = \Gamma, \qquad f'(\eta) = 1, \qquad \theta(\eta) = 1, \qquad f'''(\eta) = 0, \qquad at \quad \eta = 0, \tag{9}$$

$$f'(\eta) \to 0,\ \theta(\eta) \to 0,\ f''(\eta) \to 0, \text{ as } \eta \to \infty. \tag{10}$$

The parameters guaranteed in this model are defined and explained as follows:

$$K = \frac{2\,\Omega}{b}, \qquad \beta = \frac{\xi b}{\nu^2 \rho}, \qquad M = \frac{\sigma}{\rho b} B_0^2,$$
$$\lambda = \frac{b\,\xi u_w^2}{\kappa\nu(T_w - T_\infty)}, \qquad Ec = \frac{u_w^2}{c_p(T_w - T_\infty)},$$
$$Pr = \frac{\mu c_p}{\kappa}, \qquad \Gamma = \frac{-v_w}{\sqrt{\nu b}}.$$

We will now conclude the study by discussing the local Nusselt number Nu_x and the local skin friction coefficient Cf_x, which are important fluid dynamics parameters. They measure the rate of the HT at the surface and the shear stress exerted by the fluid on the surface, respectively. They have the following formulas, respectively:

$$Nu_x Re^{\frac{-1}{2}} = -\theta'(0), \tag{11}$$
$$Cf_x Re^{\frac{1}{2}} = -\left[f''(0) - \beta f''''(0)\right],$$

where $Re = \frac{u_w x}{\nu}$ is the local Reynolds number.

3. Implementation of the approximation method

This study seeks to examine the properties of the merged Fibonacci-Lucas polynomials (MFLPs). Additionally, we present an approximation formula for the derivatives of the MFLPs. Subsequently, employ it to resolve the provided model utilizing the least squares strategy.

3.1 Presenting the merged of FLPs

This subsection presents a novel amalgamation of FLPs and delineates certain attributes of these polynomials. The standard FLPs can be derived by applying the following two forms [25]:

$$F_i(z) - zF_{i-1}(z) - F_{i-2}(z) = 0, \qquad F_0(z) = 0, \quad F_1(z) = 1, \tag{12}$$
$$L_i(z) - zL_{i-1}(z) - L_{i-2}(z) = 0, \qquad L_0(z) = 2, \quad L_1(z) = z.$$

The forms in (12) demonstrate that both FLPs follow the same pattern; however, they begin with different initial values. Thus, we can derive the following [25]:

$$\Lambda_i(z) = z\Lambda_{i-1}(z) + \Lambda_{i-2}(z), \qquad \Lambda_0(z) = a, \quad \Lambda_1(z) = bz, \tag{13}$$

generalizes the two sets in (12). We denote $\Lambda_i(z) = FL_i^{a,b}(z)$ for the MFLPs, that is

$$FL_i^{a,b}(z) - zFL_{i-1}^{a,b}(z) - FL_{i-2}^{a,b}(z) = 0, \qquad FL_0^{a,b}(z) = a, \quad FL_1^{a,b}(z) = bz. \tag{14}$$

Theorem 3.1 Consider a positive integer i. The powerful form of impersonation of $FL_i^{a,b}(z)$ is:

$$FL_i^{a,b}(z) = \sum_{k=0}^{\lfloor \frac{i}{2} \rfloor} \frac{(i-2k+1)_{k-1}((i-2k)b + ka)}{k!} z^{i-2k}. \tag{15}$$

3.2 Approximate formula of the derivatives

The primary aim of this subsection is to provide an approximate formula for the derivatives of the MFLPs.

The function $\psi(z)$, can be approximated in terms of the MFLPs in following form:

$$\psi(z) \simeq \psi_m(z) = \sum_{\ell=0}^{m} c_\ell\, FL_\ell^{a,b}(z). \tag{16}$$

Theorem 3.2 Assume that the function $\psi(z)$ is approximated as in (16) then $D^{(n)}(\psi_m(z))$ can be defined as:

$$D^{(n)}(\psi_m(z)) = \sum_{\ell=n}^{m} \sum_{i=n}^{\lfloor \frac{\ell}{2} \rfloor} c_\ell\, \Phi_{i,\ell,n}^{a,b}\, z^{\ell-2i-n}, \tag{17}$$
$$\Phi_{i,\ell,n}^{a,b} = \frac{(\ell - 2i + 1)_{i-1}((\ell - 2\,i)b + ia)(\ell - 2i)}{i!}.$$

Proof: Having the analytic expression of the MFLPs, utilizing properties of the differential operator $D^{(n)}$, one gets the following two cases:

Case 1: For $\ell = 0, 1, \ldots, n-1$, we find $D^{(n)}\, FL_\ell^{a,b}(z) = 0$.

Case 2: For $i = n, n+1, ..., m$:

$$D^{(n)}(\psi_m(z)) = D^{(n)}\left[\sum_{\ell=0}^{m} c_\ell\, FL_\ell^{a,b}(z)\right]$$

$$= D^{(n)}\left[\sum_{\ell=0}^{m} c_\ell \sum_{i=0}^{\lfloor \frac{\ell}{2} \rfloor} \frac{(\ell-2i+1)_{i-1}((\ell-2i)b+ia)}{i!}\, z^{\ell-2i}\right]$$

$$= \sum_{\ell=0}^{m} \sum_{i=0}^{\lfloor \frac{\ell}{2} \rfloor} c_\ell \frac{(\ell-2i+1)_{i-1}((\ell-2i)b+ia)}{i!}\, D^{(n)}\, z^{\ell-2i}$$

$$= \sum_{\ell=n}^{m} \sum_{i=n}^{\lfloor \frac{\ell}{2} \rfloor} c_\ell \frac{(\ell-2i+1)_{i-1}((\ell-2i)b+ia)(\ell-2i)}{i!}\, z^{\ell-2i-n}$$

$$= \sum_{\ell=n}^{m} \sum_{i=n}^{\lfloor \frac{\ell}{2} \rfloor} c_\ell\, \Phi_{i,\ell,n}^{a,b}\, z^{\ell-2i-n},$$

where $\Phi_{i,\ell,n}^{a,b}$ is defined in (17) and this ends the proof of the required formula (17).

We will now analyze the convergence of the method proposed in this study from through the following theorem.

Theorem 3.3 Suppose that $D^{(jn)}\psi(z) \in C(0,1)$ for $j = 0, 1, \ldots, m$ and $\bar{\Psi}_m = \text{span}\left\{FL_\ell^{a,b}(z)\right\}_{\ell=0}^{m}$. If $\psi_m(z)$ defined in (16) is the best approximation (BA) to $\psi(z)$ from $\bar{\Psi}_m$ and

$$\mathbb{S}_m(\psi(z)) = \int_0^1 [\psi(z) - \psi_m(z)]^2\, dz.$$

Then

$$\lim_{m\to\infty} \mathbb{S}_m(\psi(z)) = 0.$$

Proof: To begin with, we can consider the following generalized Taylor formula:

$$\psi^*(z) = \sum_{\ell=0}^{m} \frac{z^{\ell n}}{(\ell n)!} D^{(\ell n)}\psi\left(0^+\right).$$

From this formula and $\psi^*(z) \in \bar{\Psi}_m$, one can obtain:

$$|\psi(z) - \psi^*(z)| < \frac{z^{(m+1)n}}{((m+1)n)!}\Delta_n,$$

where $\Delta_n \geq \sup_{\xi\in(0,1]} \left|D^{(mn+n)}\psi(\xi)\right|$. On account $\psi_m(z)$ is the BA of $\psi(z)$ and because of the above relation, one can get:

$$\begin{aligned} \|\psi(z) - \psi_m(z)\|_2^2 &\leq \|\psi(z) - \psi^*(z)\|_2^2 \\ &= \int_0^1 |\psi(z) - \psi^*(z)|^2 dz \\ &\leq \int_0^1 \Delta_n^2 \frac{z^{(2m+2)n}}{((mn+n)!)^2} dz \\ &= \frac{\Delta_n^2}{((mn+n)!)^2} \int_0^1 z^{(2m+2)n} dz \\ &= \frac{\Delta_n^2}{((mn+n)!)^2((2m+2)n+1)}. \end{aligned} \tag{18}$$

Therefore, one can obtain $\lim_{m\to\infty} ||\psi(z) - \psi_m(z)||_2^2 = 0$.

3.3 Numerical enforcement of the MFLPs

To utilize the MFLPs and derive the necessary framework for addressing (7)-(10) within the interval $[0, \eta_\infty] = [0, 3]$, we adhere to the subsequent stages (algorithm):

Method 1: We use the approximation by using MFLPs and the derived approximated formula of the derivatives (17) to reduce the system under study (7)-(10) to a system of algebraic equations. This will be achieved under the following three steps:

1. We estimate $f(\eta)$, and $\theta(\eta)$ by $f_m(\eta)$, and $\theta_m(\eta)$ as follows:

$$f_m(\eta) = \sum_{k=0}^{m} c_k FL_k^{a,b}(\eta), \tag{19}$$

$$\theta_m(\eta) = \sum_{k=0}^{m} d_k\, FL_k^{a,b}(\eta).$$

2. Substitution from Eqs.(17), (19) in (7)-(10), we obtain:

$$\begin{aligned} &D^{(3)}\left(f_m(\eta)\right) - \beta\, D^{(5)}\left(f_m(\eta)\right) \\ &+ \left(f_m(\eta)\right) D^{(2)}\left(f_m(\eta)\right) \\ &- \left(D^{(1)}\left(f_m(\eta)\right)\right)^2 \\ &+ (K-M)\, D^{(1)}\left(f_m(\eta)\right) = 0, \end{aligned} \tag{20}$$

$$\begin{aligned} &D^{(2)}\left(\theta_m(\eta)\right) + Pr\Big[\left(f_m(\eta)\right) D^{(1)}\left(\theta_m(\eta)\right) \\ &-k\left(\theta_m(\eta)\right) D^{(1)}\left(f_m(\eta)\right)\Big] \\ &+Ec\,\lambda\left(D^{(3)}\left(f_m(\eta)\right)\right)^2 \\ &+PrEc\left(D^{(2)}\left(f_m(\eta)\right)\right)\left(\left(D^{(2)}\left(f_m(\eta)\right)\right)\right. \\ &\left.-\beta\left(D^{(4)}\left(f_m(\eta)\right)\right)\right) = 0, \end{aligned} \tag{21}$$

$$\begin{aligned} &\sum_{k=0}^{m} c_k\, FL_k^{a,b}(0) = \Gamma, \\ &\sum_{k=0}^{m} c_k\, D^{(1)} FL_k^{a,b}(0) = 1, \\ &\sum_{k=0}^{m} d_k\, FL_k^{a,b}(0) = 1, \\ &\sum_{k=0}^{m} c_k\, D^{(3)} FL_k^{a,b}(0) = 0, \\ &\sum_{k=0}^{m} c_k\, D^{(1)} FL_k^{a,b}(\eta_\infty) = 0, \\ &\sum_{k=0}^{m} d_k\, FL_k^{a,b}(\eta_\infty) = 0, \\ &\sum_{k=0}^{m} c_k\, D^{(2)} FL_k^{a,b}(\eta_\infty) = 0. \end{aligned} \tag{22}$$

10.57647/mathsci.2026.2003.18

3. We presume that the approximate solution $(f_m(\eta), \theta_m(\eta))$ for the given problem may be supplied to perform a thorough numerical analysis via simulation. Therefore, we calculate the residual error function (REF) as outlined [26]:

$$\begin{aligned}\mathrm{REF}_1(\eta;a,b,m) &= D^{(3)}\left(f_m(\eta)\right) \\ &-\beta D^{(5)}\left(f_m(\eta)\right) + \left(f_m(\eta)\right) D^{(2)}\left(f_m(\eta)\right) \\ &-\left(D^{(1)}\left(f_m(\eta)\right)\right)^2 \\ &+(K-M)\, D^{(1)}\left(f_m(\eta)\right) \simeq 0,\end{aligned} \tag{23}$$

$$\begin{aligned}\mathrm{REF}_2(\eta;a,b,m) &= D^{(2)}\left(\theta_m(\eta)\right) \\ &+Pr\Big[\left(f_m(\eta)\right) D^{(1)}\left(\theta_m(\eta)\right) \\ &-k\left(\theta_m(\eta)\right) D^{(1)}\left(f_m(\eta)\right)\Big] \\ &+Ec\,\lambda\left(D^{(3)}\left(f_m(\eta)\right)\right)^2 \\ &+PrEc\left(D^{(2)}\left(f_m(\eta)\right)\right). \\ &\left(\left(D^{(2)}\left(f_m(\eta)\right)\right) - \beta\left(D^{(4)}\left(f_m(\eta)\right)\right)\right) \simeq 0.\end{aligned} \tag{24}$$

The smallest residual ($\mathrm{REF}_i(\eta;a,b,m) \to 0$, $i = 1,2$) signifies that the numerical solution roughly corresponds with the precise solution, indicating that the absolute error tends to zero.

Method 2: Utilizing the least squares method, we establish the objective functions:

$$SF_1[c_0, c_1, ..., c_m] = \int_0^3 [\mathrm{REF}_1(\eta;a,b,m)]\, d\eta, \tag{25}$$
$$SF_2[d_0, d_1, ..., d_m] = \int_0^3 [\mathrm{REF}_2(\eta;a,b,m)]\, d\eta.$$

To minimize $SF_1[c_0, c_1, ..., c_m]$, $SF_2[d_0, d_1, ..., d_m]$, and obtain the optimal values of c_i, d_i, $i = 0, 1, 2, ..., m$, we construct the following relations:

$$\frac{\partial SF_1}{\partial c_k} = 0, \quad \frac{\partial SF_2}{\partial d_k} = 0, \quad k = 0, 1, 2, ..., m. \tag{26}$$

Method 3: Equations (26) form a set of $(2m + 2)$ nonlinear algebraic equations that may be solved using the Newton iteration method to obtain the coefficients $\{c_k,\ d_k\}_{k=0}^{m}$. Additionally, we can determine the approximate solution of the system (7)-(10) by employing the formulas (19).

4. Validation of the numerical scheme

The MFLPs and the least squares method were utilized to numerically resolve the nonlinear ordinary differential equations and their corresponding boundary conditions. This procedure facilitated an accurate and effective study of the solution's behavior within the established boundary constraints through a methodical investigation of the problem. To validate and underscore the accuracy and consistency of our results in relation to previous studies, the skin friction coefficient, represented as $-f''(0)$, was compared with data from the literature. Hayat et al. [27] indicated that Table 1 illustrates a strong concordance between the given results and the existing literature. This consistency highlights the importance of our results in relation to previous research and affirms their validity.

Table 1. $-f''(0)$ values at various M with $K = \beta = \Gamma = 0$

M	Hayat et al. [27]	Current method
0.0	1.000000	1.0000000000
0.5	1.224747	1.2247467705
1.0	1.414217	1.4142149908
1.5	1.581147	1.5811459980
2.0	1.732057	1.7320565908

Table 2 gives an extensive discussion on numerical accuracy, convergence behavior, and error estimation of the approximation method used, which would enhance confidence in the results obtained. The residual error function was calculated at various values of the approximation order m at $\beta = 1.0$, $\lambda = 0.5$, $Ec = 0.2$, $Pr = 3.0$, $k = \Gamma = M = 1.0$. Through these comparisons, we can measure and estimate the accuracy of the proposed method. It also becomes clear that by choosing appropriate values for m, we can control the reduction of error as well as the accuracy of the proposed technique.

5. Results and discussion

The model at hand was solved by first converting the PDEs into comparable ODEs. Using the proposed technique, this transformation was completed, and the merged Fibonacci-Lucas polynomials and the least square method were then applied to solve the resulting problem. A comprehensive examination of the solutions was performed, with particular focus on the effects of altering significant parameters. This analysis elucidated how alterations to these factors influence the behavior of the system under examination. Figure 2 offers a comprehensive visual representation of the interrelated impacts on the profiles of $f'(\eta)$ and $\theta(\eta)$, as well as the variations in the stream function $f(\eta)$ across the system, illustrating how alterations in β influence the flow characteristics and thermal dynamics of the fluid. $f(\eta)$, $f'(\eta)$, and $\theta(\eta)$ increase with the growth of the couple stress parameter in this figure, suggesting that the couple stress term enhances the model's fluid flow and heat transfer. The beneficial impact of the coupled stress parameter indicates its necessity for sustaining flow stability and promoting efficient thermal energy distribution, both of which improve overall system execution.

Figure 3 illustrates the progression of $\theta(\eta)$, $f'(\eta)$, and $f(\eta)$ profiles for a specified range of M. This figure indicates that when the values of M increase, there is a notable rise in temperature near the sheet; yet, $f'(\eta)$, and $f(\eta)$ profiles exhibit entirely contrasting behavior. The MF creates the Lorentz force, which is a force that

Table 2. The REF for f, and θ via different values of m

	REF$_f$ at:			REF$_\theta$ at:		
η	$m = 4$	$m = 8$	$m = 12$	$m = 4$	$m = 8$	$m = 12$
0.0	1.9851E-05	6.2650E-08	3.5297E-10	2.3698E-05	7.9528E-08	4.5687E-10
0.75	1.0256E-05	8.0641E-08	7.0292E-10	9.0287E-05	1.9308E-08	2.6408E-10
1.5	3.0269E-05	1.9325E-07	2.9557E-10	1.2569E-05	5.8921E-08	6.8504E-10
2.25	2.3030E-04	4.0287E-07	1.9824E-09	6.0269E-04	5.9873E-07	9.2587E-09
3.0	8.6542E-04	0.1489E-07	2.0156E-09	4.6280E-04	7.9632E-07	5.3214E-09

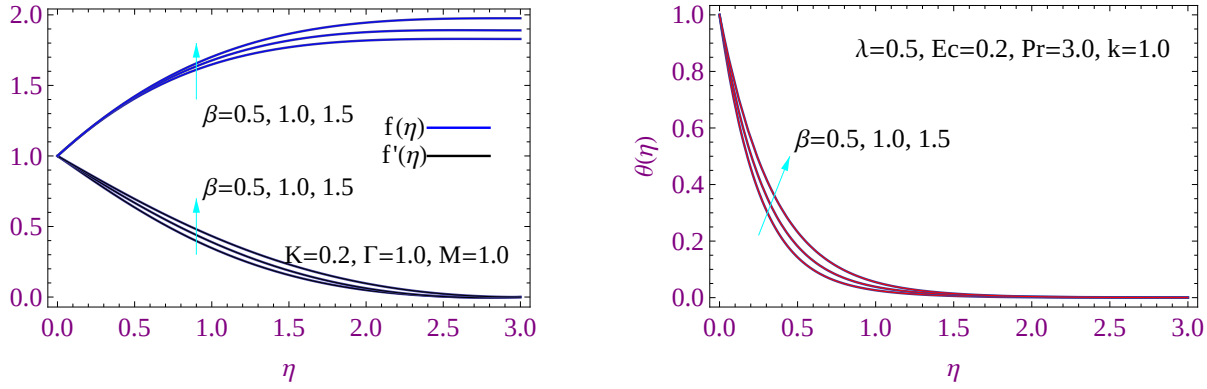

Figure 2. (a) $f(\eta)$ and $f'(\eta)$ for selected β (b) $\theta(\eta)$ for selected β.

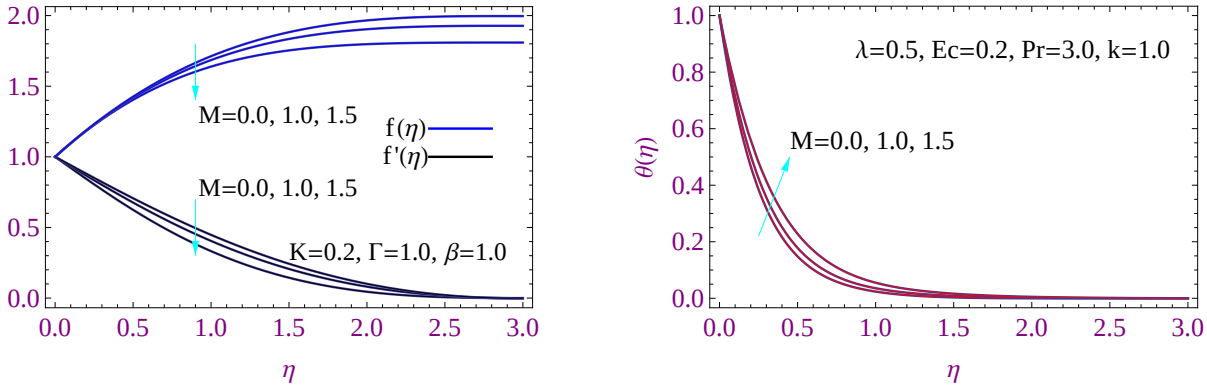

Figure 3. a) $f(\eta)$ and $f'(\eta)$ for various M (b) $\theta(\eta)$ for various M

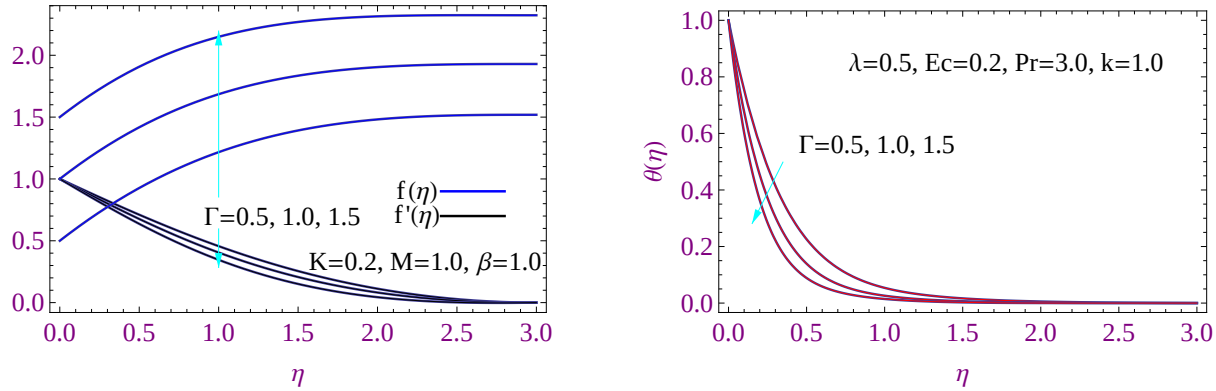

Figure 4. (a) $f(\eta)$ and $f'(\eta)$ for selected Γ (b) $\theta(\eta)$ for selected Γ

10.57647/mathsci.2026.2003.18

resists fluid motion and explains this effect. Consequently, there is a reduction in both $f'(\eta)$, and $f(\eta)$ due to the diminished fluid flow rate. The elevated thermal buildup of fluid particles is caused by the same resistive force, which increases the temperature near the sheet.

Figure 4 illustrates the dimensionless stream function $f(\eta)$, dimensionless temperature $\theta(\eta)$, dimensionless velocity $f'(\eta)$, and the influence of Γ across the boundary layer (BL). A weaker suction parameter has markedly reduced restricting effects on $f(\eta)$. A decrease in temperature and velocity fields is connected with an increase in Γ values. This is because there is more suction, which pulls fluid away from the surface and thins the BL. There is therefore less fluid available to transfer heat and momentum, which causes the velocity and temperature inside the BL to decrease.

The influence of the rotation factor K on the flow characteristics is clearly illustrated in Figure 5. As K increases, both $f(\eta)$ and $f'(\eta)$ exhibit a noticeable decline, indicating a suppression of the fluid motion and a contraction of the BL structure. This behavior is attributed to the enhanced Coriolis force induced by system rotation, which acts as a resistive mechanism opposing the primary flow direction. Consequently, the fluid particles experience a deflection and momentum loss, leading to weaker streamlines and reduced velocity magnitude. Further, the temperature field shows a significant increase with higher rotation levels. Physically, this can be explained by the reduced convective transport due to the weakened fluid motion, which limits the ability of the flow to carry heat away from the surface.

Figure 6 illustrates the influence of Ec and λ on $\theta(\eta)$. The figure shows how changes to these parameters affect the fluid's thermal behavior. Both Ec and λ exhibit an increasing trend with increasing temperature. Viscous heating reduces mechanical energy into thermal energy, and the energy couple stress refers to a fluid's internal resistance to rotational motion, facilitating energy dissipation inside the system. The total thermal energy increases as a result of these combined effects, which affects the fluid's temperature distribution.

Figure 7 illustrates the influence of Pr and k on $\theta(\eta)$ profile. The temperature profiles clearly indicate a decreasing impact of both Pr and k. A bigger temperature index parameter generally results in more rapid temperature fluctuations, reducing the overall thermal gradient. A rise in Pr signifies a larger ratio of momentum diffusivity to thermal diffusivity, resulting in a thinner thermal BL and a reduced rate of heat transfer. The confluence of these factors results in a decrease in the fluid's temperature.

Following modifications to the governing parameters, Table 3 now presents the distributions of the skin friction (SF) $Cf_x Re^{\frac{1}{2}}$ and Nusselt number (NN) $Nu_x Re^{\frac{-1}{2}}$. Assessing SF and NN is equally important, as they provide essential insights into the frictional resistance and thermal conductivity of the fluid flow. The NN assesses the efficiency of heat transfer between the fluid and the surface, whereas skin friction indicates the shear stress at the boundary, affecting the system's total drag and energy losses. Understanding these indications enhances the performance, thermal management, and efficiency of fluid flow engineering systems. An evident increase in the SF and NN correlates with a rise in the suction parameter. Decreases in the Nusselt number are significantly attributed to β, M, K, Ec, and λ. This indicates that a reduction in the rate of heat transfer between the fluid and the surface is attributable to an increase in these parameters. The table illustrates the correlation between elevated Nusselt numbers and increased Prandtl numbers, as well as temperature index Γ values. A larger temperature index value results in a steeper temperature gradient, enhancing heat transfer, whereas a higher Prandtl number facilitates thermal BL development, thereby improving heat transfer efficiency. The overall heat transfer rate between the fluid and the surface is enhanced by these parameters collectively. The table clearly indicates that higher values of the SF coefficient are attributable to β (thermal expansion coefficient), Γ (specific heat ratio), and K (thermal conductivity).

6. Conclusions

Based on the numerical results obtained from solving the problem under study by applying the approximation method used, we can summarize the following observations and recommendations, while also noting some limitations and some future suggestions:

1. Both temperature distribution and fluid velocity are positively affected by the couple stress parameter, while the suction coefficient has the opposite effect. Both the suction coefficient and the Prandtl number are also correlated with increasing the Nusselt number.

2. Increasing the suction coefficients, coupling stress, and rotation coefficient tends to an increase in the skin friction coefficients.

3. The temperature distribution can be upgraded by using lower values of the temperature index parameter or the Prandtl number.

4. The future study can investigate transient and unsteady flow scenarios to understand time-dependent thermal and flow behaviors.

Funding

This work was supported and funded by the Deanship of Scientific Research at Imam Mohammad Ibn Saud Islamic University (IMSIU) (grant number IMSIU-DDRSP2603).

Acknowledgements

This work was supported and funded by the Deanship of Scientific Research at Imam Mohammad Ibn Saud Islamic University (IMSIU) (grant number IMSIU-DDRSP2603).

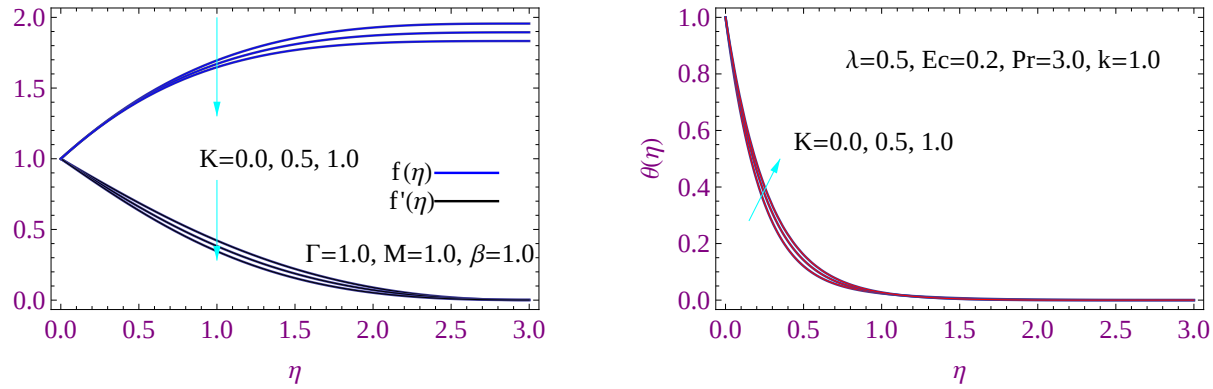

Figure 5. (a) $f(\eta)$ and $f'(\eta)$ for selected K (b) $\theta(\eta)$ for selected K

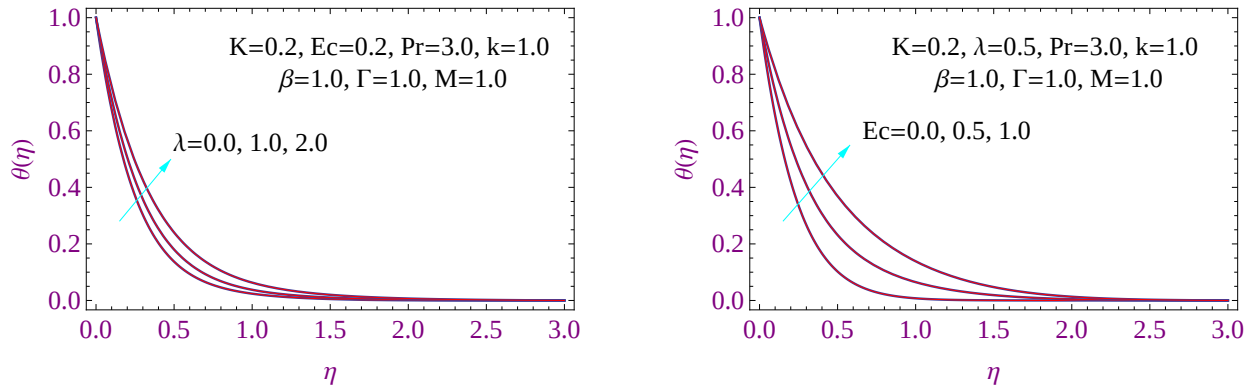

Figure 6. (a) $\theta(\eta)$ for selected λ (b) $\theta(\eta)$ for selected Ec

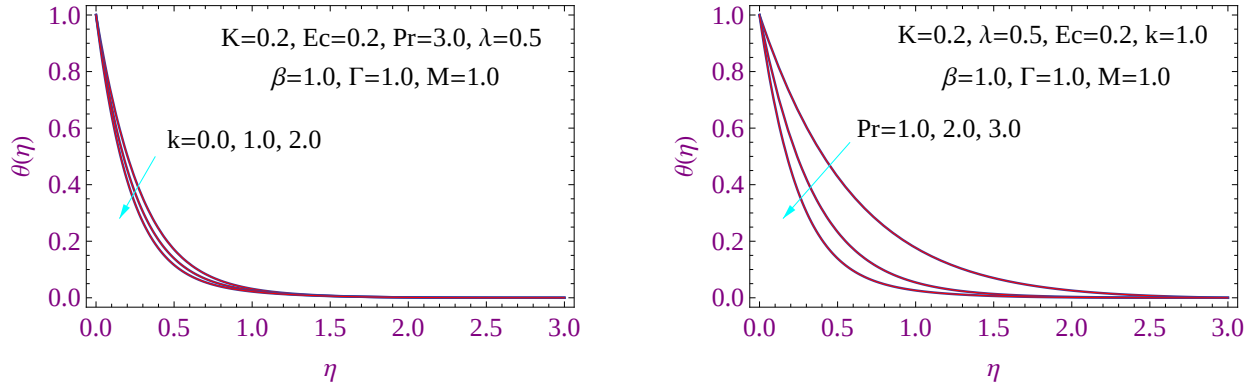

Figure 7. (a) $\theta(\eta)$ for selected k (b) $\theta(\eta)$ for selected Pr

10.57647/mathsci.2026.2003.18

Table 3. Nusselt number $Nu_x Re^{\frac{-1}{2}}$ and skin friction coefficient $Cf_x Re^{\frac{1}{2}}$ as functions of specific governing parameters

β	M	Γ	K	λ	Ec	k	Pr	$Cf_x Re^{\frac{1}{2}}$	$Nu_x Re^{\frac{-1}{2}}$
0.5	1.0	1.0	0.2	0.5	0.2	1.0	3.0	1.29016	3.84708
1.0	1.0	1.0	0.2	0.5	0.2	1.0	3.0	1.33483	3.33366
1.5	1.0	1.0	0.2	0.5	0.2	1.0	3.0	1.33558	2.81952
1.0	0.0	1.0	0.2	0.5	0.2	1.0	3.0	1.91974	3.75796
1.0	1.0	1.0	0.2	0.5	0.2	1.0	3.0	1.29998	3.35441
1.0	1.5	1.0	0.2	0.5	0.2	1.0	3.0	0.95147	2.85777
1.0	1.0	0.5	0.2	0.5	0.2	1.0	3.0	0.99090	2.80753
1.0	1.0	1.0	0.2	0.5	0.2	1.0	3.0	1.29998	3.35441
1.0	1.0	1.5	0.2	0.5	0.2	1.0	3.0	1.66333	5.04989
1.0	1.0	1.0	0.0	0.5	0.2	1.0	3.0	1.16393	4.21955
1.0	1.0	1.0	0.5	0.5	0.2	1.0	3.0	1.49378	3.84731
1.0	1.0	1.0	1.0	0.5	0.2	1.0	3.0	1.80253	3.57812
1.0	1.0	1.0	0.2	0.0	0.2	1.0	3.0	1.29898	3.89067
1.0	1.0	1.0	0.2	1.0	0.2	1.0	3.0	1.29756	3.34787
1.0	1.0	1.0	0.2	2.0	0.2	1.0	3.0	1.29653	2.78781
1.0	1.0	1.0	0.2	0.5	0.0	1.0	3.0	1.29783	4.15420
1.0	1.0	1.0	0.2	0.5	0.5	1.0	3.0	1.29783	3.00908
1.0	1.0	1.0	0.2	0.5	1.0	1.0	3.0	1.29783	2.04844
1.0	1.0	1.0	0.2	0.5	0.2	0.0	3.0	1.29960	3.30327
1.0	1.0	1.0	0.2	0.5	0.2	1.0	3.0	1.29605	3.88305
1.0	1.0	1.0	0.2	0.5	0.2	2.0	3.0	1.29596	4.38002
1.0	1.0	1.0	0.2	0.5	0.2	1.0	1.0	1.29963	1.64616
1.0	1.0	1.0	0.2	0.5	0.2	1.0	2.0	1.29791	2.81259
1.0	1.0	1.0	0.2	0.5	0.2	1.0	3.0	1.29605	3.88305

Authors contributions
All the authors have participated sufficiently in the intellectual content, conception and design of this work or the analysis and interpretation of the data (when applicable), as well as the writing of the manuscript.
Availability of data and materials
The corresponding author can furnish the data substantiating the investigation's findings upon request.
Conflict of interests
The authors stated that they possess no conflicts of interest.

References

1. Nazar R, Amin N, Filip D, and Pop I. Stagnation point flow of a micropolar fluid towards a stretching sheet. International Journal of Non-Linear Mechanics 2004; 39:1227–35. DOI: 10.1016/j.ijnonlinmec.2003.08.007
2. Ali N, Khan SU, and Abbas Z. Hydromagnetic flow and heat transfer of a Jeffrey fluid over an oscillatory stretching surface. Zeitschrift für Naturforschung A 2015; 70:567–76. DOI: 10.1515/zna-2014-0273
3. Olkha A and Dadheech A. Second law analysis for radiative MHD slip flow for two different non-Newtonian fluids with heat source. Journal of Nanofluids 2021; 10:447–61. DOI: 10.1166/jon.2021.1797
4. Nabwey HA, Alshber SI, Rashad AM, and Mahdy AEN. Influence of bioconvection and chemical reaction on magneto-Carreau nanofluid flow through an inclined cylinder. Mathematics 2022; 10:504. DOI: 10.3390/math10030504
5. Khader MM, Ahmad H, and Megahed AM. Developing some of the engineering applications through numerical treatment of non-Newtonian nanofluid flow on a nonlinear stretching surface with heat generation. Case Studies in Thermal Engineering 2023; 51:1–12. DOI: 10.1016/j.csite.2023.103641
6. Bilal M, Kolsi L, Ahmad H, Ghazwani HA, Becheikh N, and Farooq M. Numerical study of gyrotactic microorganism based on fourth-grade hybrid nanofluid flow under the influence of thermal radiation over a Riga plate. Journal of Radiation Research and Applied Sciences 2025; 18:101826. DOI: 10.1016/j.jrras.2025.101826

7. Bilal M, Riaz MB, Bajri SA, Jhangeer A, Khalifa HA, and Ahmad H. Numerical simulation of non-Newtonian hybrid nanofluid flow subject to a heterogeneous/homogeneous chemical reaction over a Riga surface. Nanotechnology Reviews 2025; 14:20240133. DOI: 10.1515/ntrev-2024-0133
8. Bilal M, Farooq M, Benghanem M, Ahmad H, and Adnan. Entropy optimization in non-Newtonian Prandtl-Eyring fluid using ANN over a curved rigid surface. International Journal of Thermal Sciences 2025; 212:109765. DOI: 10.1016/j.ijthermalsci.2025.109765
9. Bilal M, Maiz F, Farooq M, Ahmad H, Nasrat MK, and Ghazwani HA. Novel numerical and artificial neural computing with experimental validation towards unsteady micropolar nanofluid flow across a Riga plate. Scientific Reports 2025; 15:759. DOI: 10.1038/s41598-024-84480-3
10. Bilal M, Farooq M, Ahmad H, Ullah I, and Alam MM. Mathematical simulation of tangent hyperbolic-nanofluid flow coupled with a homogenous/heterogeneous chemical reaction by using Levenberg-Marquardt back propagation over a Riga plate. Journal of Thermal Analysis and Calorimetry 2025; 150:2795–809. DOI: 10.1007/s10973-024-13554-1
11. Stokes VK. Theories of Fluids with Microstructure: An Introduction. Berlin-Heidelberg-New York-Tokyo: Springer-Verlag, 1984. DOI: 10.1002/zamm.19850651204
12. Naduvinamani NB, Fathima ST, and Hiremath PS. Effect of surface roughness on characteristics of the couple stress squeeze film between anisotropic porous rectangular plates. Fluid Dynamics Research 2003; 32:217. DOI: 10.1016/S0169-5983(03)00048-0
13. Makinde OD and Eegunjobi AS. MHD couple stress nanofluid flow in a permeable wall channel with entropy generation and nonlinear radiative heat. ASME Journal of Thermal Science and Technology 2017; 12:1–17. DOI: 10.1299/jtst.2017jtst0033
14. Farooq M, Khan A, Nawaz R, Islam S, Ayaz M, and Chu YM. Comparative study of generalized Couette flow of couple stress fluid using optimal homotopy asymptotic method and new iterative method. Scientific Reports 2021; 11:3478. DOI: 10.1038/s41598-021-82746-8
15. Koriko OK, Adegbie KS, Oke AS, and Animasaun IL. Exploration of the Coriolis force on the motion of air over the upper horizontal surface of a paraboloid of revolution. Physica Scripta 2020; 95:035210. DOI: 10.1088/1402-4896/ab4c50
16. Oke AS, Mutuku WN, Kimathi M, and Animasaun IL. Coriolis effects on MHD Newtonian flow over a rotating non-uniform surface. Proceedings of the Institution of Mechanical Engineers, Part C: Journal of Mechanical Engineering Science 2021; 235:3875–87. DOI: 10.1177/0954406220969730
17. Mandala A and Sarkar A. Effect of Coriolis force on thermally radiative rotating hybrid nanofluid flow over a bi-directional stretching sheet. Hybrid Advances 2025; 10:100446. DOI: 10.1016/j.hybadv.2025.100446
18. Abd-Elhameed WM, Ahmed HM, Napoli A, and Kowalenko V. New formulas involving Fibonacci and certain orthogonal polynomials. Symmetry 2023; 15:736. DOI: 10.3390/sym15030736
19. Abd-Elhameed WM, Philippou AN, and Zeyada NA. Novel results for two generalized classes of Fibonacci and Lucas polynomials and their uses in the reduction of some radicals. Mathematics 2022; 10:2342. DOI: 10.3390/math10132342
20. Nalli A and Haukkanen P. On generalized Fibonacci and Lucas polynomials. Chaos, Solitons & Fractals 2009; 42:3179–86. DOI: 10.1016/j.chaos.2009.04.048
21. Haq S and Ali I. Approximate solution of two-dimensional Sobolev equation using a mixed Lucas and Fibonacci polynomials. Engineering with Computers 2022; 38:2059–68. DOI: 10.1007/s00366-021-01327-5
22. Khan NA, Riaz F, and Khan NA. Heat transfer analysis for a couple stress fluid over a nonlinearly stretching sheet. Nonlinear Engineering 2013; 2:121–7. DOI: 10.1515/nleng-2013-0014
23. Islam S and Zhou CY. Exact solutions for two dimensional flows of couple stress fluids. Zeitschrift für Angewandte Mathematik und Physik 2007; 58:1035–48. DOI: 10.1007/s00033-007-5075-5
24. Megahed AM. Improvement of the heat transfer mechanism through a Maxwell fluid flow over a stretching sheet embedded in a porous medium and convectively heated. Mathematics and Computers in Simulation 2021; 187:97–109. DOI: 10.1016/j.matcom.2021.02.018
25. Abd-Elhameed WM and Alqubori OM. New expressions for certain polynomials combining Fibonacci and Lucas polynomials. AIMS Mathematics 2025; 10:2930–57. Available from: [aimspress.com](https://www.aimspress.com/article/doi/10.3934/math.2025136
26. Parand K and Delkhosh M. Operational matrices to solve nonlinear Volterra-Fredholm integro-differential equations of multi-arbitrary order. Gazi University Journal of Science 2016; 29:895–907

27. Hayat T, Mustafa M, and Pop I. Heat and mass transfer for Soret and Dufour's effect on mixed convection boundary layer flow over a stretching vertical surface in a porous medium filled with a viscoelastic fluid. Communications in Nonlinear Science and Numerical Simulation 2010; 15:1183–96. DOI: 10.1016/j.cnsns.2009.05.062

28. Juma BA, Oke AS, Mutuku WN, Ariwayo AG, and Ouru OJ. Dynamics of Williamson fluid over an inclined surface subject to Coriolis and Lorentz forces. Engineering and Applied Science Letters 2022; 5:37–46. DOI: 10 . 30538 / psrp - easl2022 . 0083